PHYSICAL REVIEW B VOLUME 43, NUMBER 4 1 FEBRUARY 1991

Structural and magnetic properties of Er thin films and Er/Y superlattices: Magnetoelastic effects

J.A. Borchers* and M.B. Salamon
Department of Physics and Materials Research Laboratory, University of Illinois at Urbana-Champaign, 1110 West Green Street, Urbana, Illinois 61801

R.W. Erwin and J.J. Rhyne
National Institute of Standards and Technology, Gaithersburg, Maryland 20899

R.R. Du and C.P. Flynn
Department of Physics and Materials Research Laboratory, University of Illinois at Urbana-Champaign, 1110 West Green Street, Urbana, Illinois 61801

(Received 1 August 1990; revised manuscript received 5 October 1990)

Crystalline erbium thin films and Er/Y superlattices with varying Er-layer thicknesses have been grown by molecular-beam epitaxy. The magnetic and structural properties of these samples have been analyzed by x-ray-scattering, bulk magnetization, and neutron-diffraction techniques. From a comparison of the data for the two systems, the importance of interfacial strain relative to artificial modulation in shaping the magnetic behavior has been determined. Though the basic nature of the erbium magnetic order is not qualitatively altered in either the thin films or superlattices, the conical ferromagnetic phase is suppressed in all of the samples considered. The enhanced critical fields exhibit a systematic dependence on Er-layer thickness. These effects appear to follow directly from the epitaxial basal-plane strain which is measurable in films over 14 000 Å thick. This strain, along with a "clamping" of the Er thermal expansion to the Y lattice, leads to a reduction of the magnitude of the magnetoelastic energy that drives the ferromagnetic transition. The dependence of the magnetoelastic energy on the epitaxial strain is described by a model which accounts for the elastic coupling of the erbium lattice to the yttrium.

I. INTRODUCTION

The development of molecular-beam epitaxy and other controlled deposition techniques has sparked extensive investigations of materials with tailored structural, electronic, and magnetic properties. There exists special interest in magnetic superlattice systems such as Gd/Y,[1] Dy/Y,[2] and Fe/Cr,[3] in which the effects of the epitaxy on the bulk magnetic properties and the origin of the layer coupling are still not well understood. This paper details the structural and magnetic properties of one such system, erbium-yttrium superlattices, and complementary Er thin films with varying Er-layer thicknesses. Specifically, we examine modifications of the Er magnetic phases that follow directly from the interfacial lattice matching. The commensurate spin states are discussed in a companion paper.[4]

A. Background

Interest in artificially modulated metallic materials arose as early as the 1920's. Subsequently many attempts have been made to identify interfacial effects and improve interface quality in order to make use of the novel properties of ideal structurally modulated materials.[5,6] Interdiffusion, leading to sinusoidal chemical modulation of the component materials,[7] has been a recurring problem. Coherence of Cu/Nb sputtered multilayers along the growth direction was achieved and modeled by Schuller.[8] In the early 1980's Durbin *et al.*[9] synthesized metal superlattices with full three-dimensional order using molecular-beam epitaxy (MBE). This technique was later applied to the growth of magnetic rare-earth superlattices.[10]

Epitaxially grown Gd/Y superlattices,[1,11] while showing a systematic reduction of the Gd moment from interfacial mixing, demonstrated the presence of Gd-spin coupling across the nonmagnetic interlayers. Because its sign depends on yttrium thickness, the interaction was associated with Ruderman-Kittel-Kasuya-Yosida (RKKY) coupling via the Y conduction band. Concurrent investigations of Dy/Y superlattices[2] indicated that the basal-plane spiral of bulk dysprosium also propagates through the nonmagnetic interlayers. None of the superlattices considered showed evidence of the first-order ferromagnetic transition observed in bulk Dy.[12] This suppression is due to the inhibition of magnetoelastic distortions that drive the transition resulting from growth-induced clamping of the basal-plane strains.

B. Properties of the constituent materials

As background for the Er/Y superlattice and Er thin-film study presented here, we first consider the properties of the component materials. Both erbium and yttrium crystallize in a hexagonal close-packed structure. Despite a 2.5% lattice mismatch, coherent epitaxial growth is possible. While yttrium is not a rare-earth metal, its electronic configuration is so similar that it behaves like a rare earth with no magnetic moment [$\chi \leq 10^{-5}$ emu/g (Ref. 13)]. Comparable to the magnetic rare earths, the yttrium band structure leads to a distinct peak in the generalized susceptibility $\chi(\mathbf{q})$ at $q = 0.375\pi/c$ ($\approx 67°$/layer).[14] Dilute magnetic rare-earth–yttrium alloys indeed order in spiral phases with a turn angle at T_N that approaches 50°/layer.[15]

In contrast bulk Er has a complex magnetic structure.[16] It is paramagnetic above $T_N = 85$ K. For $52 < T < 85$ K the spins are sinusoidally modulated along the c axis. In the region $20 < T < 52$ K, a basal plane spiral develops with a turn angle matching that of the c-axis modulation (CAM). The c-axis and basal-plane order "square up" as the temperature is decreased.[17] Finally at $T_C = 20$ K, there is a first-order transition to the conical c-axis ferromagnetic state. This transition is accompanied by uniform compression of the basal plane and an expansion of the c axis.[18] At 6 K the moment components of $\mu_{\|}$ and $\mu_{\perp}$ are $7.80\mu_B$ and $4.44\mu_B$, respectively,[17] corresponding to a semicone angle of 29.6° and a maximum moment close to the $9.0\mu_B$ value predicted for the $J = \frac{15}{2}$ spin system. The magnetization as a function of the c-axis field was measured by Feron.[19] The critical field H_C, which marks the transition from the c-axis modulated state to the aligned spin phase, increases with temperature to a maximum value of 22.4 kOe at 67 K.

II. EXPERIMENTAL TECHNIQUES AND DATA ANALYSIS

A. Sample growth

All of the samples considered in this study were grown in a Perkin Elmer 400 molecular-beam-epitaxy chamber at the University of Illinois, using growth procedures detailed elsewhere.[2,20] The general structures of the thin films and superlattices are shown in Fig. 1. The samples were grown on 1.2 cm^2×0.6 mm crystalline sapphire with the [11$\bar{2}$0] axis perpendicular to the growth plane. To inhibit the reactivity of the rare-earth materials with the substrate, an 800–1200-Å buffer layer of [110] Nb was deposited from an e-beam gun at a temperature of 900 °C. A second e-beam gun was used to grow a base layer of [0002] yttrium (300–600 Å) at a temperature near 700 °C. For the thin-film samples shown in Fig. 1(a), a [0002] erbium layer ranging among samples from 375 to 14 500 Å was then deposited from an effusion cell and capped with 20–40 Å of Y. For the superlattice samples shown in Fig. 1(b), the growth of ≈ 100 alternating layers of Er and Y, each on the order of 50 Å, was controlled by computerized shutters. The growth rate for both the thin films and superlattices was stabilized near 0.5 Å/sec. The sample thickness was monitored during growth by a quartz oscillator and a mass spectrometer. At various stages of growth, the crystalline quality was checked by reflection high-energy electron diffraction. The substrate temperature was held close to 425 °C for the superlattices and near 450 °C for the thin films. Postgrowth thickness measurements were made using a linear profilometer.

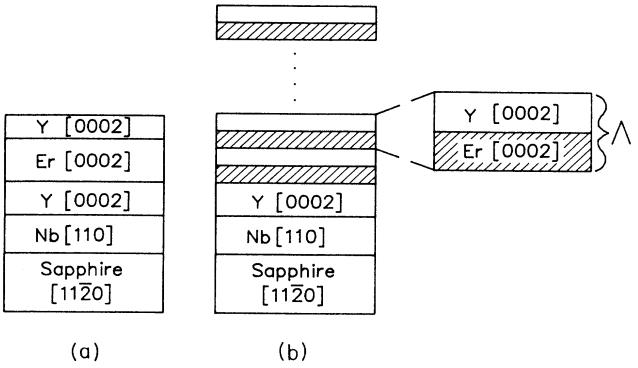

FIG. 1. Schematic drawing of (a) an Er thin film and (b) an Er/Y superlattice. In (b) the parameter Λ designates the thickness of a single superlattice bilayer.

B. Bulk magnetization measurements

All of the magnetization studies were performed on a standard, commercial superconducting quantum interference device (SQUID) based magnetometer. Field-cooled and zero-field-cooled magnetization of the Er samples was measured as a function of temperature at fields up to 50 kG. The moments were normalized by the sample mass determined by multiplying the Er volume by the bulk Er density. Because of thickness irregularities and edge effects, the volume estimates are uncertain by 5% to 10%. The moments of the sapphire substrate and gelatin sample holder were determined by fitting and subtracting the Er Curie-Weiss contribution above T_N; these diamagnetic corrections were subtracted from all subsequent data.

Because the field was applied perpendicular to the sample face, a demagnetizing field of the form $-4\pi NM$ arises. For thin-film samples, N should equal one. However, the demagnetization factors that give the sharpest vertical jump when the Er spins align take values smaller than unity, as shown in Table I. ($N = 1$ causes the data to be double valued as a function of internal field.) For all samples except the 3950-Å film, these parameters are approximately equal to the ratio of the Er thickness to the combined Er and Y thickness (Refer to Tables II and III). These deviations from $N = 1$ will be discussed in the context of epitaxial strain in Section V C.

TABLE I. Demagnetization factors for the Er thin films and Er/Y superlattice samples extracted from the magnetization vs field data. The elastic coupling parameters r_z were estimated from a comparison of the critical fields for the epitaxial samples in Table IV to the theoretical calculations of $\Delta\mu H_C$ from Eq. (18). The volume ratio of yttrium to erbium is given for comparison to r_z.

Sample	N	V_Y/V_{Er}	r_z	$\frac{1}{1+r_z}$
3950-Å film	1	0.126	0.085	0.922
9500-Å film	0.96 ± 0.05	0.032	0.105	0.905
3900-Å film	0.89 ± 0.04	0.115		
14 500-Å film	0.87 ± 0.05	0.152		
1750-Å film	0.82 ± 0.15	0.223	0.388	0.720
860-Å film	0.69 ± 0.07	0.395	0.455	0.687
375-Å film	0.68 ± 0.20	0.467		
$[Er_{31.5}\,|Y_{21}]_{60}$	0.59 ± 0.10	0.694	2.45	0.290
$[Er_{23.5}\,|Y_{19}]_{100}$	0.54 ± 0.04	0.852	1.53	0.395
$[Er_{25.5}\,|Y_{25.5}]_{80}$	0.48 ± 0.05	1.04		
$[Er_{13.5}\,|Y_{25}]_{100}$	0.34 ± 0.10	1.91	1.82	0.355

C. Experimental diffraction analysis

X-ray-diffraction studies were performed on the thin films and superlattices to provide room-temperature structural information. The x-ray measurements were done on a double axis diffractometer equipped with a fine focus Cu tube and a graphite monochromator positioned after the sample. The in-plane mosaic spread of the scattering crystal was extracted from rocking curves through the (0002) and (0004) reflections. Extensive 2θ scans were also performed along the [000l] direction through the (0002) and (0004) peaks. The resolution of the diffractometer was determined by measuring the full width at half maximum of the resolution-limited sapphire substrate peak.

To explore the magnetic order in the samples, neutron-scattering experiments were carried out at the National Institute of Standards and Technology on a standard triple axis spectrometer. A pyrolytic graphite monochromator was set to select neutrons at a wavelength of 2.4616 Å (equivalent to an energy of 13.5 meV). A (002) pyrolytic graphite analyzer crystal was used to decrease the background signal. Collimation of 40′-25′-25′-40′ provided instrument resolution $\Delta K_l \leq 0.022$ Å^{-1} along the [000l] direction and transverse resolution $\Delta K_t = 0.002$ Å^{-1} near the Er (0002) reflection. For low-temperature scans the sample was mounted with its growth plane perpendicular to the scattering plane on the cold finger of a controlled-flow cryostat. For this study, scans were done along the [000l] direction through the (0002) peak in reflection geometry and through the $(10\bar{1}0)$ or the $(10\bar{1}1)$ peak in transmission geometry.

Both the x-ray and neutron intensities were corrected for absorption and geometrical effects (Lorentz factor). For the x-ray data analysis the absorption coefficient μ was set equal to the weighted average of the x-ray absorption coefficients for Er and Y, 1212 cm^{-1} and 597 cm^{-1}, respectively.[21] The absorption coefficients for neutron scattering lead to corrections of less than 0.1% and were neglected. The Lorentz correction[22] for the x-ray scans with constant angular velocity is simply $\mathcal{L} = \frac{1}{\sin 2\theta}$ and for the neutron scans with constant $\mathbf{K}$ steps is $\mathcal{L} = \frac{1}{\sin\theta}$. To account for the angular divergence of the neutron beam allowed by the collimators and the mosaic spreads of the sample, monochromator, and analyzer, the Lorentz

TABLE II. The Er film thicknesses and Y base layer thicknesses were measured by linear profilometer techniques. The c-axis coherence lengths, c-axis lattice parameters, and crystalline mosaics were determined from room-temperature x-ray scans. The 10-K a-axis and c-axis lattice parameters were calculated from the positions of the neutron structural reflections.

		X ray at room temperature			Neutron at 10 K	
Er layer (Å)	Y base layer (Å)	Coherence (Å)	Mosaic (deg)	c (Å)	a (Å)	c (Å)
375 ± 40	175 ± 25	328	0.493	5.577		
860 ± 50	340 ± 25	582	0.336	5.576	3.580	5.559
1750 ± 50	390 ± 50	587	0.324	5.572	3.578	5.562
3900 ± 150	450 ± 50	803	0.274	5.581		
3950 ± 100	500 ± 50	1078	0.368	5.596	3.554	5.578
9500 ± 100	300 ± 50	1041	0.196	5.588	3.555	5.577
14 500 ± 500	2200 ± 200	1033	0.275	5.582		

TABLE III. The layer thicknesses of the Er and Y were determined from linear profilometer measurements and from the x-ray superlattice peaks. The mosaic spreads, c-axis coherence lengths and average c-axis spacings were measured by x-ray-diffraction techniques. c-axis parameters in the Er and Y portions of each bilayer were extracted from fits of the (0002) x-ray scans to the damped wave model. The a-axis spacings were determined from the positions of the $(10\bar{1}0)$ or $(10\bar{1}1)$ neutron reflections at 10 K. The 10-K c-axis spacings were extracted from fits of the (0002) neutron data to the damped wave model.

		X ray at room temperature				Neutron at 10 K	
Superlattice sample	Er Layer / Y Layer (Å)	Mosaic (deg)	Coherence (Å)	c_{ave} (Å)	c_{Er}/c_Y (Å)	a_{ave} (Å)	c_{Er}/c_Y (Å)
$[Er_{31.5}\,\vert Y_{21}]_{60}$	87.5 ± 2.0	0.291	774	5.637	5.574	3.5970	5.531
	60.7 ± 2.0				5.729		5.716
$[Er_{23.5}\,\vert Y_{19}]_{100}$	65.5 ± 3.0	0.350	761	5.662	5.572	3.5970	5.529
	55.8 ± 3.0				5.780		5.716
$[Er_{25.5}\,\vert Y_{25.5}]_{80}$	71.2 ± 3.0	0.448	1060	5.662	5.562		
	73.7 ± 3.0				5.753		
$[Er_{13.5}\,\vert Y_{25}]_{100}$	38.0 ± 4.0	0.284	640	5.704	5.555	3.6024	5.519
	72.5 ± 4.0				5.778		5.758

correction was multiplied by factors derived by Axe and Hastings.[23]

D. Structure-factor determination

The angular positions and intensities of the peaks in the x-ray- and neutron-diffraction scans can be determined using the theory of elastic scattering from a crystal lattice. The general expression for the nuclear scattered intensity is

$$I_{\text{nuc}}(\mathbf{K}) \propto P\left|\sum_i b_i(\mathbf{K})e^{i\mathbf{K}\cdot\mathbf{R}_i}\right|^2 , \tag{1}$$

where $\mathbf{K}$ is the scattering vector and $\mathbf{R}_i$ is the position of the ith scattering atom. For neutron diffraction the scattering amplitude $b_i(\mathbf{K})$ is independent of angle and equals 0.775×10^{-12} cm and 0.803×10^{-12} cm for yttrium and erbium, respectively.[24] The polarization factor P is equal to one. For x-ray scattering the approximate functional form of $b_i(\mathbf{K})$ is given in the *International Tables for X-ray Crystallography*,[25] and $P = (1+\cos^2 2\theta)/2$. Evaluation of Eq. (1) for a simple crystal indicates that nuclear peaks occur at $\mathbf{K} = \mathbf{G}$ where $\mathbf{G}$ is a reciprocal-lattice vector.

For neutron diffraction the magnetic scattering simply adds to the nuclear contribution. In the elastic limit the magnetic intensity has the general form

$$I_{\text{mag}}\mathbf{K} \propto \sigma_m^2 \sum_{\alpha,\beta}(\delta_{\alpha,\beta} - \hat{K}_\alpha\hat{K}_\beta)\left(\sum_{\mathbf{r}}\mathcal{F}^*(\mathbf{K})e^{-i\mathbf{K}\cdot\mathbf{r}}\langle S_\alpha(\mathbf{r})\rangle\right)\left(\sum_{\mathbf{r}'}\mathcal{F}(\mathbf{K})e^{i\mathbf{K}\cdot\mathbf{r}'}\langle S_\beta(\mathbf{r}')\rangle\right) , \tag{2}$$

where $\sigma_m = 0.2695\times10^{-12}$ cm, $\langle S_{\mathbf{r}}^\alpha\rangle$ is the magnetic moment in Bohr magnetons at site $\mathbf{r}$, and $\hat{K}_\alpha$ is the unit scattering vector in the α direction. The factor $(\delta_{\alpha,\beta} - \hat{K}_\alpha\hat{K}_\beta)$ is zero when the scattering vector is parallel to the moment direction. The magnetic scattering amplitude $\mathcal{F}(\mathbf{K})$ was calculated by Blume, Freeman, and Watson[26] for the rare-earth ions.

Three magnetic structures are of interest in this study: ferromagnetic alignment, basal-plane helix and c-axis spin modulation. For a ferromagnet with all of the spins aligned along $\hat{\mathbf{z}}$, temperature-dependent peaks add to the nuclear intensity unless the scattering vector $\mathbf{K}$ is parallel to the z axis. For the case of a basal-plane helix with the modulation wave vector $\mathbf{Q}$ parallel to $\hat{\mathbf{z}}$, magnetic peaks develop to either side of the nuclear reflections at $\mathbf{K} = \mathbf{G} \pm \mathbf{Q}$. The satellite intensities are largest when $\mathbf{K}$ is parallel to the z axis. In the final case of a sinusoidal CAM with wave vector $\mathbf{Q} \parallel \hat{\mathbf{z}}$, peaks appear to either side of the Bragg reflections at $\mathbf{K} = \mathbf{G}\pm\mathbf{Q}$, but no scattering occurs when $\mathbf{K}$ is parallel to $\hat{\mathbf{z}}$. As the CAM "squares up," additional magnetic reflections develop at $\mathbf{K} = \mathbf{G} \pm m\mathbf{Q}$ where m is an odd integer.

To describe the scattering from the Er/Y superlattices, the nuclear and magnetic structure factor calculations [Eqs. (1) and (2)] are extended to a c-axis modulated system with $\mathcal{N}$ total bilayers, each consisting of N_A atomic layers of element A and N_B layers of element B ($N_T = N_A + N_B$). It is initially assumed that the system is rectangle-wave modulated with a wavelength $\Lambda = N_A c_A + N_B c_B$, where c_A is the c-axis spacing of el-

ement A and c_B is the spacing of B. For a one-atom basis and $\mathbf{K} \parallel \hat{\mathbf{z}}$, Eq. (1) leads to

$$I(\mathbf{K}) \propto \left| \left(\sum_n e^{inK\Lambda} \right) \left(\sum_{m=0}^{N_T-1} b_m e^{iKz_m} \right) \right|^2 . \quad (3)$$

In this expression z_m is the c-axis position of the mth atomic plane with respect to the start of the nth bilayer; $z_m = mc_A$ for $0 \leq m < N_A$ and $z_m = N_A c_A + (m - N_A)c_B$ for $N_A < m < N_T$. The scattering length b_m exhibits similar behavior. As described for the Dy/Y superlattices,[2] the scattered intensity consists of a series of narrow peaks spaced at multiples of the superlattice wave vector $K_{\rm SL} = \frac{2\pi n}{\Lambda}$, modulated by a broad envelope function. This function selects reflections near $K_{\rm SL} = \frac{2\pi m}{c_{\rm ave}}$ where $c_{\rm ave} = \frac{\Lambda}{N_T}$. The lattice mismatch ($c_A \neq c_B$) leads to an asymmetrical arrangement of the surrounding superlattice sidebands.

To calculate the magnetic intensity for a superlattice with c-axis modulated moments parallel to the c axis, we take $\langle S_z(n\Lambda + z_m) \rangle = \langle S_m \rangle \sin(n\Phi + \phi_m)$, where Φ is the total CAM phase shift across each bilayer and ϕ_m is the phase shift at site m with respect to the beginning of each bilayer. The bilayer phase shift can be written $\Phi = N_A Q_A c_A + N_B Q_B c_B$ where Q_A is the wave vector of the magnetic modulation in element A and Q_B is the wave vector in B. Assuming that element B is nonmagnetic (i.e., $\langle S_z^B \rangle = 0$), we can write an expression for the magnetic intensity:

$$I_{\rm mag}(\pm\mathbf{Q}) \propto \tfrac{1}{4}\sigma_m^2(1 - \hat{K}_z^2) \left| \left(\sum_n e^{inK\Lambda \pm in\Phi} \right) \left(\sum_{m=0}^{N_A-1} \langle S_z^A \rangle \mathcal{F}_m(\mathbf{K}) e^{iKz_m \pm i\phi_m} \right) \right|^2 . \quad (4)$$

The first summation produces a series of peaks at $K_{\rm mag}^{\pm} = K_{\rm SL} \pm \frac{\Phi}{\Lambda}$. The second summation is an envelope function that selects out the magnetic reflections near $K_{\rm mag} = \frac{2\pi m}{c_A} \pm Q_A$. The peaks that result from the nuclear and magnetic structure factor calculations above are summarized in the inset of Fig. 7.

Due to diffusion and step formation at the interfaces, real metallic superlattices are not perfectly rectangle-wave modulated. To treat them, we use a damped rectangle-wave model[2] in which successive Fourier components of the rectangle wave are reduced by damping factors. For Er/Y superlattice systems, the model is modified to account for the gradual squaring of the CAM as the temperature is decreased. Specifically the c-axis moment in the jth layer of the superlattice is written[27]

$$\langle \mathbf{S}_z(j,\delta) \rangle = \mathcal{C}_A(j,\alpha) \frac{\langle S_z^A \rangle}{\arctan[\exp(-\delta)]} \times \sum_{m=0}^{\infty} \frac{e^{-(2m+1)\delta}}{2m+1} \sin[(2m+1)\phi_z(j,\gamma)]\hat{\mathbf{z}} \quad (5)$$

where $\mathcal{C}_A(j,\alpha)$ is the concentration of element A in the jth layer and $\phi_z(j,\gamma)$ is the total CAM phase shift in the jth layer reduced by damping factors α and γ, respectively. If $\delta = 0$, the CAM is rectangle-wave modulated, and as δ approaches infinity the variation becomes sinusoidal. The basal-plane spiral, which coexists with the CAM at low temperatures, is more simply described by the following:

$$\langle \mathbf{S}_{x,y}(j) \rangle = \mathcal{C}_A(j,\alpha) \langle S_{x,y}^A \rangle \{ \cos[\phi_{x,y}(j,\gamma)]\hat{\mathbf{x}} + \sin[\phi_{x,y}(j,\gamma)]\hat{\mathbf{y}} \} . \quad (6)$$

The neutron- and x-ray-diffraction data for the Er/Y superlattices were fit to expressions obtained by substituting Eqs. (5) and (6) along with similar series for the c-axis spacing, concentration, and phase shift profiles into the nuclear and magnetic structure factors given by Eqs. (1) and (2), respectively.

III. Er THIN FILMS

A. Structural characterization

To examine the modification of the magnetic properties resulting from the epitaxial constraints, seven Er thin films were studied using the bulk magnetization and diffraction techniques described in the previous section. Their characteristics are listed in Table II. Notice that two of the films have a nominal thickness of 4000 Å. The 3950-Å film was grown at a faster rate of 0.8 Å/sec and deposited on a sapphire substrate with a miscut of 1.1° with respect to the $(11\bar{2}0)$ plane. (The usual miscut is less than 0.5°.) This sample exhibits reduced strain relative to the 3900-Å film, possibly because the sapphire ledges promote the formation of structural domain boundaries. Room-temperature x-ray scans for each sample show narrow peaks corresponding to the (0002) Er, the (0002) Y, the (110) Nb and the $(11\bar{2}0)$ sapphire lattice reflections. No spurious scattering is evident. The room-temperature c-axis lattice parameters determined from the (0002) Er reflections are listed in Table II. With the exception of the thicker films, the values are somewhat smaller than the bulk Er parameter of 5.595 Å. (The 3950-Å film is fully relaxed to the bulk lattice constant.) Table II also lists the c-axis structural coherence lengths calculated

from the integrated widths of the (0002) reflections. The thicker films are highly ordered single crystals with coherence lengths greater than 1000 Å. For most of the samples, the mosaic spreads in Table II are better than 0.37°, a value comparable to other metallic crystals.

B. Magnetic properties

Neutron-diffraction and bulk magnetization measurements detailed elsewhere[28,29] show that the films are paramagnetic at high temperatures, have a c-axis modulated spin structure in the intermediate-temperature region and have a basal-plane spiral coexisting with the CAM at low temperatures comparable to bulk Er. A series of neutron scans through the $(10\bar{1}0)$ reflection are shown in Fig. 2 for the 3950-Å film at temperatures between 10 and 65 K. The central peak at $K_z = 0$ is the structural Bragg reflection. As illustrated in the inset of Fig. 7, the CAM gives rise to the $(10\bar{1}0)^+$ and $(10\bar{1}0)^-$ peaks separated from the Bragg reflection by $\Delta K_z = 0.298$ Å^{-1} at 10 K. The presence of the $(10\bar{1}1)^{-3}$ and $(10\bar{1}\,\bar{1})^{+3}$ third-order magnetic reflections at $K_z = \pm 0.232$ Å^{-1} indicates that the CAM approaches square-wave modulation below 35–40 K in a manner similar to bulk. In scans along the $[000l]$ direction, magnetic $(0002)^{\pm}$ reflections develop below $T_{N\perp} \approx 45$ K signaling the growth of a basal-plane spiral with the same periodicity as the CAM. Neutron data for the 9500-, 1750-, and 860-Å films have similar features. The CAM coherence length is greater than 250 Å for the 860- and 1750-Å films and ranges from 350 to 600 Å for the 3950- and 9500-Å films. For these four films the spiral coherence lengths are comparable.

C. Suppression of the ferromagnetic transition

One of the most dramatic differences between the thin films and elemental erbium is the absence of the conical ferromagnetic spin phase. This suppression is signaled by the absence of low-temperature ferromagnetic scattering at zero field for the 860-, 1750-, 3950- (Refer to Fig. 2), and 9500-Å Er films. Further, low-field magnetization measurements show no evidence of a first-order transition in films up to 14 500 Å thick.

In bulk erbium, the ferromagnetic transition is accompanied by an abrupt compression of the basal-plane lattice parameters (< 0.2%) and a sharp c-axis expansion. The a-axis spacings for the thin films obtained by neutron-diffraction techniques do not vary with temperature; they are clamped by the epitaxy. In addition, the parameters are slightly larger than the bulk Er values at low temperatures. The a-axis spacings at 10 K for four of the thin films are listed in Table II. Neutron scans for the 860-Å film at 10 and 50 K along the K_x direction actually show evidence of two peaks to either side of the central $(11\bar{2}0)$ reflection. The lattice spacings calculated from these reflections are 3.565 and 3.596 Å in comparison to the Er and Y values [3.554 Å (Ref. 30) and 3.644 Å (Ref. 31), respectively]. Apparently the a-axis spacing is not entirely uniform through each film.

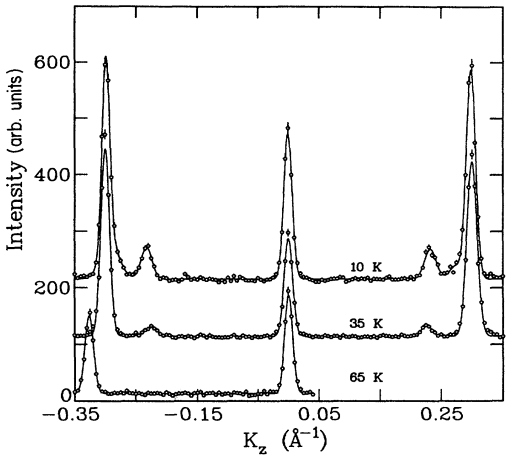

FIG. 2. Neutron-diffraction scans along the $[10\bar{1}l]$ direction for the 3950-Å film at 10, 35 and 65 K. The $(10\bar{1}0)^{\pm}$ CAM magnetic satellites are evident at $K_z = \pm 0.298$ Å^{-1}. The smaller reflections located near $K_z = \pm 0.232$ Å^{-1} are the third-order magnetic satellites of the $(10\bar{1}1)$ and $(1\bar{0}11)$ reflections.

The stretching of the basal-plane lattice leads to a compression of the films along the c-axis direction. The temperature dependence of the c-axis parameters for the 860-, 1750-, and 9500-Å films is shown in Fig. 3, along

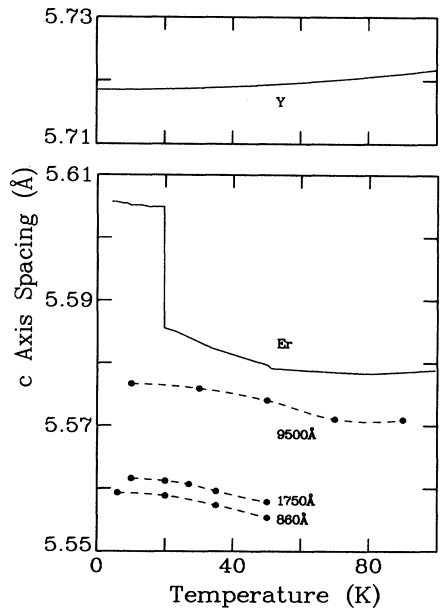

FIG. 3. The top graph shows the c-axis spacings for bulk yttrium determined by extrapolating data from Finkel (Ref. 31) to low temperatures. The c-axis lattice parameters for the 860-, 1750-, and 9500-Å Er thin films are plotted as a function of temperature in the bottom graph. The spacings were calculated from the positions of the (0002) neutron reflections. The lattice parameters for bulk Er (Ref. 30) are plotted for comparison.

with those of bulk Er (Ref. 30) and Y.[31] With the exception of the 3950-Å film, both the a-axis and c-axis spacings systematically approach the bulk spacing as the thickness is increased. Figure 3 also shows that the c axis of each Er film, being only partially clamped, expands as the temperature is decreased following the trend of bulk Er. The anomalous 0.35% jump at T_C, however, is absent.

D. Field dependence

The field dependence of the magnetization for the thin-film systems gives further insight into the role of clamping and strain at the Er/Y interface. In Fig. 4 the c-axis magnetization for the 9500-Å Er film is plotted versus internal field at various temperatures. While these data are qualitatively similar to the bulk data,[19] there is significant enhancement of the fields that mark the transition to the aligned spin state. In Fig. 5 the critical fields extracted from data similar to that in Fig. 4 are plotted as a function of film thickness at 10 and 20 K. A linear extrapolation of the 20-K data suggests that a 2-μm film is required to recover bulk behavior. The critical fields measured for two of the films, however, do not fit the thickness trend. At 10 K the H_C value of 2.7 kOe for the 3950-Å film is even smaller than the value of 3.1 kOe for the 9500-Å film. In contrast, the 5.0-kOe critical field at 10 K for the 14 500-Å film is somewhat larger than the value for the 9500-Å film. In Sec. V we will show that the critical fields closely follow the degree of epitaxial strain irrespective of film thickness.

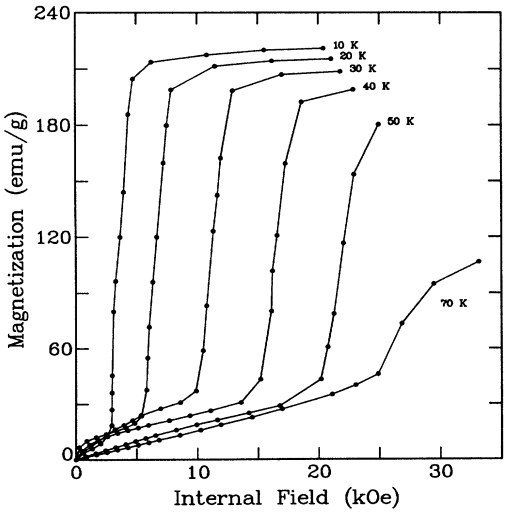

FIG. 4. Field dependence of the magnetization for the 9500-Å Er film at various temperatures. The c-axis fields have been corrected for demagnetization effects as described in Sec. II B.

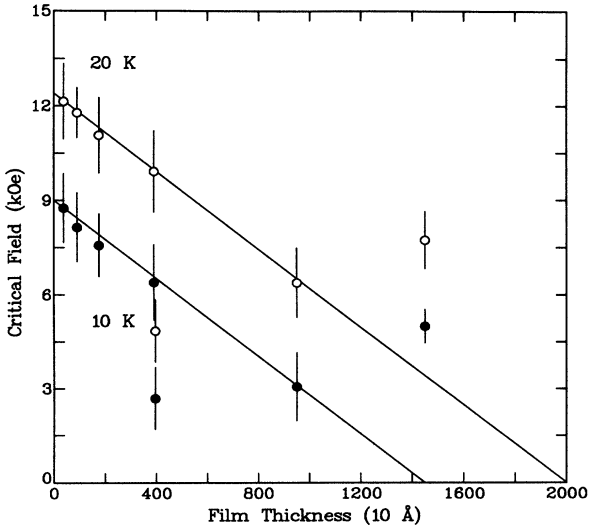

FIG. 5. Critical field vs Er film thickness at 10 K (solid circles) and 20 K (open circles). The critical fields were obtained from plots of the magnetization vs field for each film. The solid lines mark linear extrapolations of the data to $H_C = 0$ kOe.

IV. ER/Y SUPERLATTICES

A. Structural characterization

The thin-film results serve as a basis for studies of Er/Y superlattices. The four samples studied were $[Er_{13.5}|Y_{25}]_{100}$, $[Er_{13.5}|Y_{25}]_{100}$, $[Er_{31.5}|Y_{21}]_{60}$, and $[Er_{25.5}|Y_{25.5}]_{80}$,[32] with Er thicknesses ranging from 35 to 90 Å per bilayer and Y thicknesses from 55 to 75 Å per bilayer. The thickness of the Er and Y layers in each sample, determined from linear profilometer measurements, is listed in Table III. Figure 6 shows a typical room-temperature x-ray scan about the (0002) reflection for the sample $[Er_{23.5}|Y_{19}]_{100}$. The position of the central reflection gives an average c-axis lattice spacing of 5.662 Å, which is between the values of 5.595 and 5.741 Å for Er and Y, respectively. Table III lists c_{ave} for all of the superlattices, along with the c-axis coherence lengths calculated from the integrated widths of the (0002) Bragg reflections. In general structural domains extend over more than five superlattice bilayers. The mosaic spreads (Table III) determined from rocking curves through the (0002) peak are less than 0.45°; the quality of the superlattices is comparable to other metallic crystals. The central Bragg reflection in Fig. 6 is surrounded by intense superlattice sidebands visible up to fifth order. These peaks have nearly the same width as the centroid, indicating that the bilayer wavelength of 120.3 Å is constant through the entire sample.

In order to obtain more specific information about the structure and composition of the superlattices near the interfaces, the x-ray data were fit to the damped rectangle-wave model. The resulting c-axis spacings in

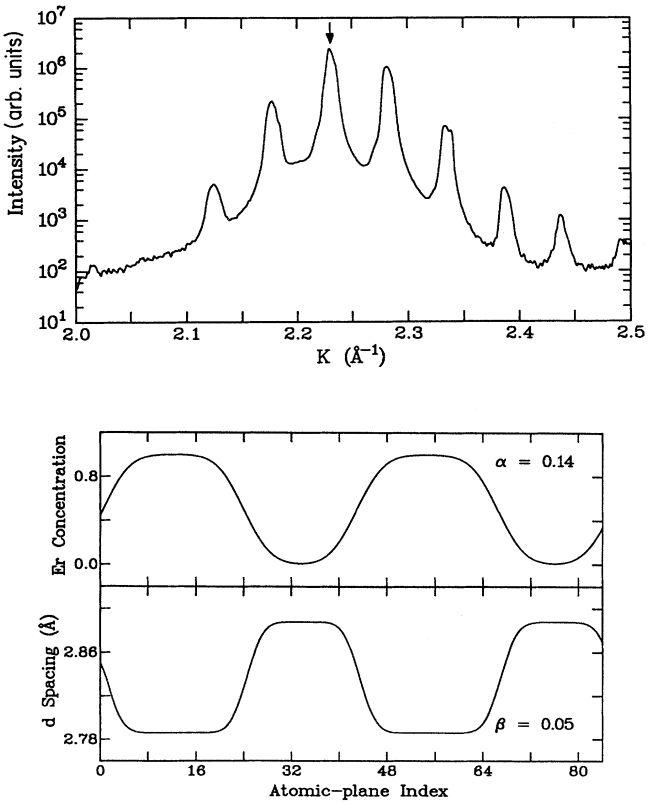

FIG. 6. Room-temperature x-ray-diffraction scan through the (0002) reflection for $[Er_{23.5}|Y_{19}]_{100}$. The arrow marks the central Bragg peak. The surrounding harmonics (up to fifth order) result from the 120.3-Å wavelength of the superlattice. The bottom graph shows the concentration (volume fraction) of Er per atomic layer and the d-spacing profile obtained from fits of this scan to the damped rectangle-wave model.

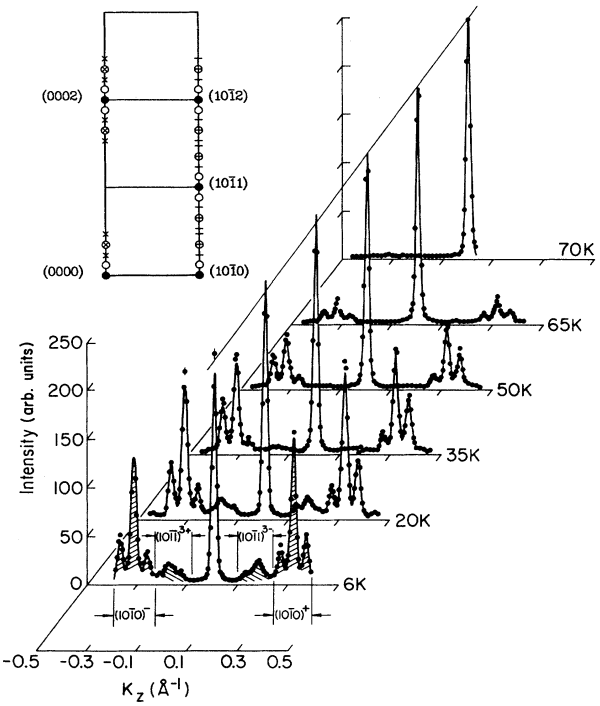

FIG. 7. Neutron-diffraction scans along the $[10\bar{1}l]$ direction for $[Er_{23.5}|Y_{19}]_{100}$ at temperatures ranging from 6 to 70 K. The CAM magnetic satellites and superlattice sidebands are labeled $(10\bar{1}0)^+$ and $(10\bar{1}0)^-$. $(10\bar{1}\,\bar{1})^{3+}$ and $(10\bar{1}1)^{3-}$ are the third-order magnetic satellites of the $(10\bar{1}\,\bar{1})$ and $(10\bar{1}1)$ reflections, respectively. The inset represents the structure factor for an Er/Y superlattice in reciprocal space. • marks the structural reflections and o corresponds to their superlattice sidebands. ⊗ indicates the magnetic satellites and surrounding superlattice peaks (×) arising from the development of the basal-plane spiral. ⊕ marks the CAM reflections and their sidebands (+).

the Er and Y layers are given in Table III. The Er parameters are slightly smaller and the Y spacings are somewhat larger than the respective bulk values. A typical modulation profile obtained for $[Er_{23.5}|Y_{19}]_{100}$ is plotted in Fig. 6. The interface region extends over fewer than five layers, while the corresponding d-spacing modulation is quite abrupt.

B. Magnetic properties

The detailed nature of the spin order in the superlattices was investigated using bulk magnetization[28,33] and neutron-diffraction techniques.[27] Figure 7 shows a series of zero field scans through the $(10\bar{1}0)$ reflection for $[Er_{23.5}|Y_{19}]_{100}$ at temperatures ranging from 6 to 70 K. The largest peak visible is the structural Bragg reflection at $K_x = (2\pi/a)(2/\sqrt{3})$, $K_z = 0$, where a is approximately equal to 3.581 Å at all temperatures. Magnetic peaks separated from the central peak by $\Delta K_z \approx 0.315$ Å^{-1} confirm the existence of a sinusoidal CAM below $T_{N\|} \approx 78$ K. These peaks, along with their accompanying superlattice harmonics, are labeled $(10\bar{1}0)^+$ and $(10\bar{1}0)^-$ in Fig. 7. The peaks marked $(10\bar{1}\,\bar{1})^{3+}$ and $(10\bar{1}1)^{3-}$ correspond to the third-order magnetic harmonics of the $(10\bar{1}\,\bar{1})$ and the $(10\bar{1}1)$ structural reflections, respectively.

A similar series of scans through the (0002) reflection are shown for $[Er_{23.5}|Y_{19}]_{100}$ in Fig. 8 at temperatures ranging from 6 to 35 K. The central peak is the structural Bragg reflection located near $K_z = 2\pi/c_{ave}$. Two superlattice sidebands are separated from this peak by $\Delta K_z = 2\pi n/\Lambda$ with $\Lambda = 120.2$ Å. The cross-hatched groups labeled $(0002)^+$ and $(0002)^-$ are magnetic satellites of the central peak along with their superlattice harmonics, which mark the existence of a basal-plane spiral below $T_{N\perp} \approx 28$ K. Interference from the sapphire substrate restricts scans to the range shown.

The coherence lengths of the CAM and the basal-plane spiral were calculated for $[Er_{23.5}|Y_{19}]_{100}$, $[Er_{13.5}|Y_{25}]_{100}$, and $[Er_{31.5}|Y_{21}]_{60}$ from the widths of the $(10\bar{1}0)^{\pm}$ or $(10\bar{1}1)^{\pm}$ and $(0002)^{\pm}$ reflections, respectively, after deconvoluting the instrument resolution and structural broadening. The coherence length of the CAM ranges from 200 Å for $[Er_{13.5}|Y_{25}]_{100}$ to 300 Å

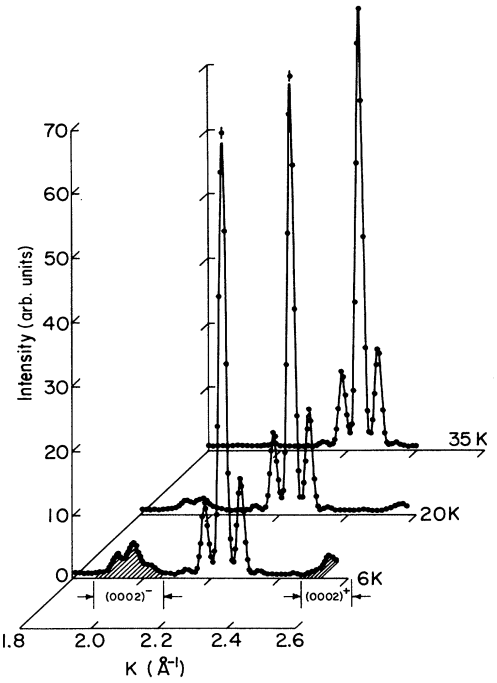

FIG. 8. Neutron-diffraction scans along the [000l] direction for $[Er_{23.5}|Y_{19}]_{100}$ at temperatures ranging from 6 to 35 K. The central (0002) structural reflection is surrounded by superlattice sidebands. The magnetic satellites and accompanying superlattice sidebands labeled $(0002)^+$ and $(0002)^-$ mark the existence of a basal-plane spiral.

for $[Er_{31.5}|Y_{21}]_{60}$, while the spiral coherence varies only from 150 to 200 Å. The coherence length is larger than the bilayer wavelengths in each superlattice, implying that the magnetic order is not interrupted by the nonmagnetic yttrium interlayers.

C. Suppression of the ferromagnetic transition

As with the Er films, no low-temperature ferromagnetic scattering is evident in Fig. 7 at the central Bragg position. The c-axis ferromagnetic phase is apparently suppressed for $[Er_{23.5}|Y_{19}]_{100}$ and the other superlattice samples. Bulk magnetization data support this result.

To explain this phenomenon, we again compare the strain profiles to bulk Er and Y. The a-axis lattice spacings of the superlattices extracted from neutron measurements show little variation with temperature; like the Er films, they are clamped by the epitaxy. Table III lists their 10-K values, which fall between the bulk Er and Y spacings. It is noted that the presence of only a single lattice peak in the K_x neutron scans indicates that the basal-plane lattice parameters are constant through each sample, in contrast to the films.

The uniform stretching of the basal plane in the superlattices leads to a compression of the Er lattice along the c-axis direction. The values of the c-axis lattice parameters in the individual Er and Y layers were extracted from fits of the [000l] and [10$\bar{1}l$] neutron scans to the damped rectangle-wave model. The Er and Y spacings are both independent of temperature. In particular, the 0.35% expansion of the bulk Er c axis at T_C is not observed in the superlattice data. The 10-K c-axis spacings in the Er and Y layers for $[Er_{31.5}|Y_{21}]_{60}$, $[Er_{23.5}|Y_{19}]_{100}$, and $[Er_{13.5}|Y_{25}]_{100}$ are given in Table III. As expected, the Er parameters are all significantly smaller than the corresponding bulk value of 5.605 Å.

D. Magnetic field dependence

The bulk magnetization for $[Er_{23.5}|Y_{19}]_{100}$ is plotted in Fig. 9 as a function of c-axis internal field at temperatures ranging from 10 to 60 K. The saturation moment obtained by extrapolating the high-field moment to zero field is 208 emu/g for $[Er_{23.5}|Y_{19}]_{100}$ at 10 K in comparison to 269 emu/g for bulk Er and 210–220 emu/g for the Er thin films. The other superlattices studied show similar moment reductions. Below 30 K saturation occurs in two stages: a plateau for $H \leq 17$ kOe and $T \leq 30$ K followed by a step increase at a critical field H_C. (The plateau is explained in the context of commensurate spin structures in the companion paper.[4]) In Fig. 10 the critical fields extracted from Fig. 9 and similar graphs for $[Er_{13.5}|Y_{25}]_{100}$ and $[Er_{31.5}|Y_{21}]_{60}$ are plotted versus temperature along with results for bulk Er.[19] (The values for $[Er_{25.5}|Y_{25.5}]_{80}$ are not shown, but are virtually identical to those obtained for $[Er_{23.5}|Y_{19}]_{100}$.) The superlattice fields are clearly much larger and less temperature dependent than bulk, though they do not follow the Er thickness trend suggested by the thin-film data in Fig. 5. Instead, the critical fields of both the films and

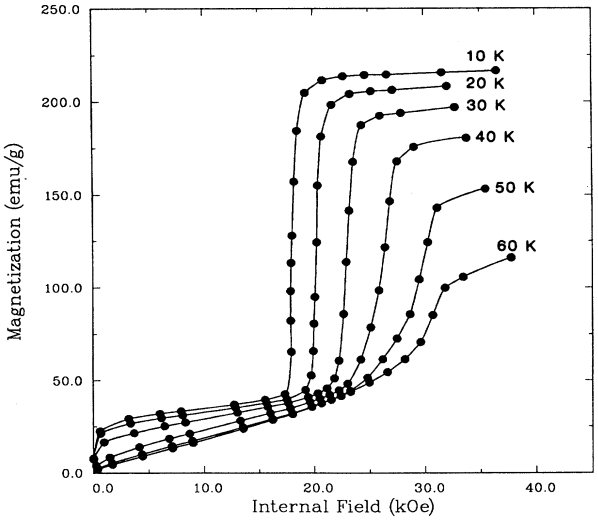

FIG. 9. Field dependence of the magnetization for $[Er_{23.5}|Y_{19}]_{100}$ at various temperatures. The c-axis fields have been corrected for demagnetization effects as discussed in Sec. II B.

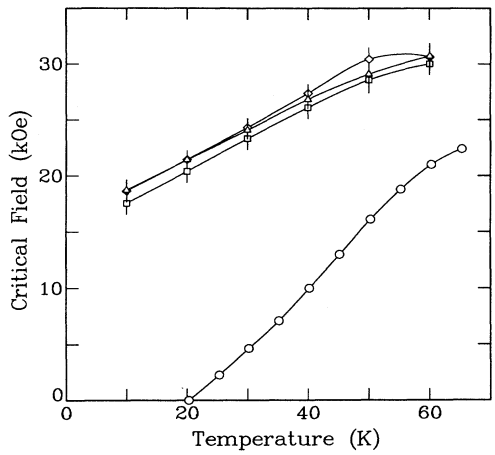

FIG. 10. Critical field plotted as a function of temperature for $[Er_{23.5}|Y_{19}]_{100}$ (squares), $[Er_{13.5}|Y_{25}]_{100}$ (diamonds), and $[Er_{31.5}|Y_{21}]_{60}$ (triangles). The bulk Er values (circles) are shown for comparison.

superlattices appear to increase linearly with the degree of epitaxial lattice strain. This dependence is described in the following section.

V. ANALYSIS

The bulk magnetization and neutron-diffraction results presented above show that the magnetic properties of the thin-film and superlattice systems are altered in a consistent manner. An examination of the rare-earth energetics indicates that the epitaxial strain evident in both systems is primarily responsible for the novel magnetic behavior. In this section the general Hamiltonian for the magnetic rare earths is reviewed with emphasis on the competition between the exchange and magnetoelastic energies that drives the ferromagnetic transition in bulk erbium. The modification of the magnetoelastic energy caused by the elastic coupling of the Er lattice to the Y lattice is then modeled and compared to the critical-field data.

A. Hamiltonian for the rare earths

The complicated magnetic phases of bulk erbium and other rare earths result from competing spin interactions which are modeled by the generalized Hamiltonian:

$$\mathcal{H} = \mathcal{H}_{\rm ex} + \mathcal{H}_{\rm CF} + \mathcal{H}_{\rm ME} \ . \tag{7}$$

$\mathcal{H}_{\rm ex}$ is the long-range exchange among the $4f$ moments that gives rise to the spin modulation, and $\mathcal{H}_{\rm CF}$ is the anisotropy. The magnetoelastic term $\mathcal{H}_{\rm ME}$ is a combination of the elastic energy and the magnetoelastic interaction that follows from the strain dependence of the crystal field (single-ion contribution) and the exchange (two-ion contribution). In general the magnetoelastic energy and anisotropy favor ferromagnetic spin alignment at the expense of lattice distortions. The competition between these interactions and the exchange term drives the first-order ferromagnetic transition in bulk erbium.

In a phenomenological treatment, the magnetoelastic energy in Cartesian coordinates can be written

$$E_{\rm ME} = \tfrac{1}{2}\sum_{i,j} c_{ij}\epsilon_{ii}\epsilon_{jj} - \sum_j K_j\epsilon_{jj} \ , \tag{8}$$

where the ϵ_{jj} terms are the irreducible strains, the c_{ij} coefficients are the elastic stiffness constants, and the K_j terms are the magnetoelastic coefficients that depend on the one- and two-spin correlation functions.[34] The equilibrium strains and energy, obtained by minimizing $E_{\rm ME}$ with respect to the strains, satisfy the following equations:

$$K_i = \sum_j c_{ij}\bar{\epsilon}_{jj} \ , \tag{9}$$

$$\overline{E}_{\rm ME} = -\tfrac{1}{2}\sum_{ij} c_{ij}\bar{\epsilon}_{ii}\bar{\epsilon}_{jj} = -\tfrac{1}{2}\sum_j K_j\bar{\epsilon}_{jj} \ . \tag{10}$$

The elastic coefficients have been measured by Rosen[35] and are listed in the Appendix along with the anomalous Er strains above and below T_C determined by Rhyne.[18] The Appendix also includes the K_j coefficients for bulk Er calculated from Eq. (9). Following the treatment by Rosen,[35] the driving energy at the transition evaluated from Eq. (10) is equal to

$$\Delta\overline{E}_{\rm ME} = \overline{E}^{f}_{\rm ME} - \overline{E}^{a}_{\rm ME} = -1.01\ {\rm J/cm^3} \ , \tag{11}$$

favoring ferromagnetism. It is assumed that this energy is equal to the exchange energy barrier at T_C together with additional dipolar corrections.[36]

B. Epitaxial modifications of the magnetoelastic energy

The suppression of the ferromagnetic transition and the enhanced critical fields follow from changes in the magnitude of $\Delta\overline{E}_{\rm ME}$ relative to the exchange. In bulk Er the ferromagnetic transition is driven primarily by a reduction of the exchange interaction through the two-ion terms in the magnetoelastic energy. Jensen[36] argues that the exchange energy is altered in the epitaxial systems by the lattice strain resulting from the Er and Y mismatch. To estimate the magnitude of this effect, we assume perfect epitaxy and treat each Er-Y sample as a coupled elastic system sharing a common lattice parameter in the interfacial plane. We add to Eq. (8), therefore, the elastic energy contribution $E^{\rm Y}_{\rm ME}$ from the yttrium lattice:[37]

$$E^{\rm Y}_{\rm ME} = r_z\sum_{ij} \tfrac{1}{2}\tilde{c}_{ij}\tilde{\epsilon}_{ii}\tilde{\epsilon}_{jj} \ , \tag{12}$$

where $\tilde{c}_{ij}$ are the elastic constants for the Y lattice and $\tilde{\epsilon}_{jj}$ are the Y strains relative to the paramagnetic Er strains. The parameter r_z describes the degree to which the Er lattice parameter approaches that of Y and, absent clamping to the substrate, equals the Y/Er volume ratio. For epitaxy, the basal-plane lattice parameters of the Er and Y are constrained to be equal. The yttrium basal-plane strains can then be written,

$$\begin{aligned} \tilde{\epsilon}_{xx} &\approx \epsilon_{xx} - \epsilon_{0x,y} \ , \\ \tilde{\epsilon}_{yy} &\approx \epsilon_{yy} - \epsilon_{0x,y} \ , \end{aligned} \tag{13}$$

where the mismatch $\epsilon_{0x,y}$ between the Er and Y lattice is equal to 0.025. These constraints are substituted into the general expression for $E_{\rm ME}$, and the result is minimized with respect to the c-axis Y strain to give the following expression for the energy per unit volume of Er:

$$\begin{aligned} E_{\rm ME} = {} & \tfrac{1}{2}c_{11}(\epsilon_{xx}^2 + \epsilon_{yy}^2) + c_{12}\epsilon_{xx}\epsilon_{yy} + \tfrac{1}{2}c_{33}\epsilon_{zz}^2 + c_{13}\epsilon_{zz}(\epsilon_{xx} + \epsilon_{yy}) \\ & + r_z\left(\tfrac{1}{2}c_{11}[(\epsilon_{xx} - \epsilon_{0x,y})^2 + (\epsilon_{yy} - \epsilon_{0x,y})^2] + c_{12}(\epsilon_{xx} - \epsilon_{0x,y})(\epsilon_{yy} - \epsilon_{0x,y}) - \frac{1}{2}\frac{c_{13}^2}{c_{33}}(\epsilon_{xx} + \epsilon_{yy} - 2\epsilon_{0x,y})^2\right) \\ & - K_x\epsilon_{xx} - K_y\epsilon_{yy} - K_z\epsilon_{zz} \ , \end{aligned} \tag{14}$$

where it is assumed that both materials have identical elastic constants. Minimizing this expression with respect to the Er strains, we obtain the following relationships for the equilibrium strain $\bar{\epsilon}_{zz}$:

$$\bar{\epsilon}_{zz} = \frac{K_z - c_{13}(\bar{\epsilon}_{xx} + \bar{\epsilon}_{yy})}{c_{33}} \tag{15}$$

and for $\bar{\epsilon}_{xx}$ and $\bar{\epsilon}_{yy}$

$$\bar{\epsilon}_{xx} + \bar{\epsilon}_{yy} = \frac{\hat{K} + 2r_z\hat{c}\epsilon_{0x,y}}{\hat{c}(1 + r_z)}, \tag{16}$$

where

$$\begin{aligned} \hat{c} &\equiv c_{11} + c_{12} - 2\frac{c_{13}^2}{c_{33}} \ , \\ \hat{K} &\equiv K_x + K_y - 2\frac{c_{13}}{c_{33}}K_z \ . \end{aligned} \tag{17}$$

Upon substitution of these expressions Eq. (14) becomes

$$\bar{E}_{\rm ME} = -\frac{1}{2}\left(\frac{(\hat{K} + 2r_z\hat{c}\epsilon_{0x,y})^2}{2\hat{c}(1 + r_z)}\right) + r_z\hat{c}\epsilon_{0x,y}^2 - \frac{1}{2}\frac{K_z^2}{c_{33}}, \tag{18}$$

assuming that $\bar{\epsilon}_{xx} = \bar{\epsilon}_{yy}$.

In the case of bulk Er, $r_z = 0$, and $\bar{E}_{\rm ME}$ reduces to the following:

$$\bar{E}_{\rm ME} = -\frac{1}{2}\left(\frac{\hat{K}^2}{2\hat{c}}\right) - \frac{1}{2}\frac{K_z^2}{c_{33}}, \tag{19}$$

as previously demonstrated in Eqs. (9) and (10). At the other extreme of $r_z = \infty$, the lattice expansion of the Er is strongly clamped to the Y, and

$$\begin{aligned} \bar{\epsilon}_{xx} &= \epsilon_{0x,y} \ , \\ \bar{\epsilon}_{zz} &= \frac{K_z}{c_{33}} - 2\frac{c_{13}}{c_{33}}\epsilon_{0x,y} \ . \end{aligned} \tag{20}$$

The resulting magnetoelastic energy is equal to

$$\bar{E}_{\rm ME} = \hat{c}\epsilon_{0x,y}^2 - \hat{K}\epsilon_{0x,y} - \frac{1}{2}\frac{K_z^2}{c_{33}}. \tag{21}$$

Notice that the driving energy $\Delta\bar{E}_{\rm ME}$ exhibits linear dependence on the lattice mismatch $\epsilon_{0x,y}$.

For the epitaxial systems, the measured critical fields are proportional to the difference between the ferromagnetic and antiferromagnetic magnetoelastic energy relative to the exchange barrier (Eq. (11)]:

$$\Delta\mu H_C = \Delta\bar{E}_{\rm ME} + 1.01 \ {\rm J/cm^3} \ , \tag{22}$$

where $\Delta\mu$ is the difference between the moment of the antiferromagnetic state and the saturated state. In Fig. 11,

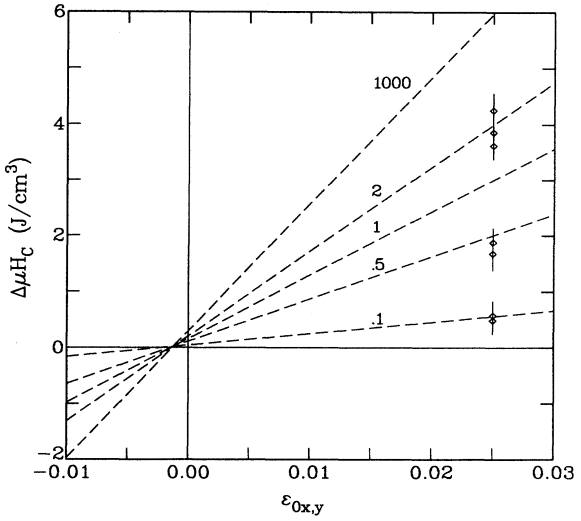

FIG. 11. $\Delta\mu H_C$ calculated from Eq. (18) for the elastic coupling model. The lines correspond to $r_z = 0.1$, 0.5, 1, 2, and 1000 as marked. The case of bulk Er is equivalent to $\Delta\mu H_C = 0$. For comparison, the energy equivalents of the critical fields from Table IV are plotted as a function of the lattice mismatch.

$\Delta\mu H_C$ calculated from Eq. (18) using the magnetoelastic parameters in the Appendix is plotted as a function of $\epsilon_{0x,y}$ at values of r_z ranging from 0 [Eq. (19)] to 1000 [Eq. (21)]. Note that the r_z dependence vanishes when the mismatch is equal to $(\hat{K}_a + \hat{K}_f)/4\hat{c}$. The energy increases sharply as both the coupling to the Y and the lattice mismatch parameter $\epsilon_{0x,y}$ are increased. Table IV lists the $T = 0$ K critical fields and their energy equivalents ($\Delta\mu H_C$) for several thin films and superlattices extracted from the bulk magnetization measurements described in Sec. III D and IV D. (For the superlattices $\Delta\mu$ is roughly $\frac{6}{7}$ of the saturation moment as suggested by Fig. 9.) These data are also plotted in Fig. 11 at the Er-Y mismatch value of 0.025. The values of r_z obtained from this treatment, and listed in Table I, are comparable to the volume ratio of Y to Er (V_Y/V_{Er}) as expected. Note that the critical fields could potentially be lowered by growth on a substrate with a smaller mismatch.

For completeness the measured strain dependence of the critical fields is compared to $\Delta\mu H_C$ calculated as a function of the antiferromagnetic c-axis strain. Replacing $\epsilon_{0x,y}$ in Eq. (18) in terms of $\bar{\epsilon}_{zz}$ from Eqs. (15) and (16), we obtain

$$\Delta\overline{E}_{\rm ME} = -\frac{(\hat{K}^f - \hat{K}^a)^2}{4\hat{c}(1+r_z)} + \frac{(\hat{K}^a - \hat{K}^f)}{2c_{13}}(K_z^a - c_{33}\bar{\epsilon}_{zz}^a) + \frac{(K_z^a)^2 - (K_z^f)^2}{2c_{33}}, \quad (23)$$

where f and a designate the ferromagnetic and antiferromagnetic values of the coefficients, respectively. Because the explicit r_z dependence in this expression is negligible, $r_z = 1000$ is assumed for simplicity. Figure 12 shows $\Delta\mu H_C$ as a function of $\bar{\epsilon}_{zz}$ calculated from Eq. (23) using the elastic and magnetoelastic coefficients for bulk Er listed in the Appendix. On the same graph, the experimental values of $\Delta\mu H_C$ for the films and superlattices are plotted versus the c-axis anomalous strains, which are listed in Table IV along with the a-axis strains. Note that the experimental and theoretical energies both vary linearly with lattice strain. The model calculation matches the data reasonably well except for the two points corresponding to the superlattices $[Er_{23.5}\,|Y_{19}]_{100}$ and $[Er_{13.5}\,|Y_{25}]_{100}$. The c-axis parameters for these samples were extracted from fits of the neutron diffraction data to the damped rectangle-wave model described in Sec. II D and are subject to uncertainties that are not indicated. Clearly, the modification of the magnetoelastic energy induced by the elastic coupling of the Er lattice to the Y is responsible for the suppression of the ferromagnetic transition and the critical-field enhancement. The controlling factor is the homogeneous lattice strain which, judging by Fig. 5, is determined by factors such as film thickness and growth conditions.

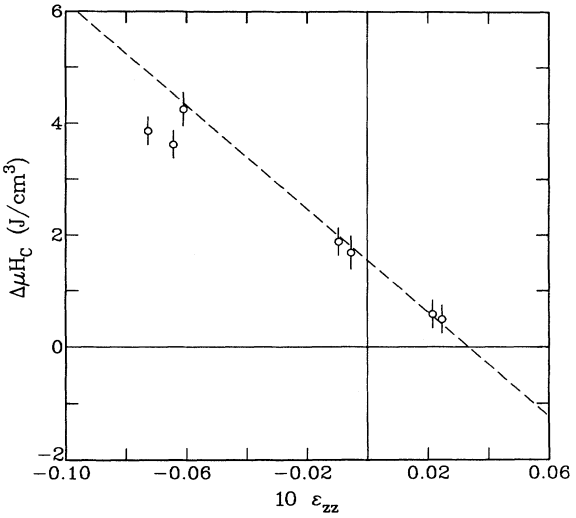

FIG. 12. The energy equivalent of the 0-K critical fields for the epitaxial Er systems vs the c-axis lattice strain. The dashed line corresponds to $\Delta\mu H_C$ calculated from Eq. (23) as a function of $\bar{\epsilon}_{zz}$ with $r_z = 1000$.

C. Strain dependence of the demagnetizing field

As described in Sec. II B, the effective demagnetization factors are significantly lower than the predicted value of 1.0 and depend on the relative Er content of the samples. The inconsistent value of N obtained for the strain relieved 3950-Å film, however, suggests that the demagnetization factor is actually determined by the degree of epitaxial strain similar to the critical fields. A comparison of the N values listed in Table I with the corresponding strains in Table IV indicates that the demagnetization factor systematically decreases as the basal plane

TABLE IV. The a-axis and c-axis strains at 10 K were calculated from the parameters in Tables II and III relative to the bulk Er values of 3.56 Å and 5.595 Å, respectively. The table also gives the critical fields at 0 K and their energy equivalents.

Sample	ϵ_{xx} ($\times 10^{-3}$)	ϵ_{zz} ($\times 10^{-3}$)	H_C at 0 K (kOe)	$\Delta\mu H_C$ (J/cm^3)
3950 Å	−0.703	2.47	1.83	0.49
9500 Å	−0.453	2.16	2.16	0.58
1750 Å	5.96	−0.541	6.25	1.68
860 Å	6.77	−0.953	7.00	1.88
$[Er_{31.5}\,|Y_{21}]_{60}$	12.95	−6.10	18.00	4.25
$[Er_{23.5}\,|Y_{19}]_{100}$	11.43	−6.43	16.50	3.62
$[Er_{13.5}\,|Y_{25}]_{100}$	11.43	−7.27	17.80	3.86

is stretched to match the Y. The empirical values of N roughly agree with $1/(1+r_z)$ (Table I) calculated using the r_z values estimated from Fig. 11. Since the lattice coupling parameter r_z is ideally equal to the ratio of the volume of Y to Er, this correlation is consistent with the observed thickness dependence of N.

The crystal symmetry dependence of the dipole-dipole contribution to the energy was examined as a possible explanation for these strain and r_z correlations. Estimates of the total dipolar energy by Jensen[36] imply that deviations of the crystal lattice from the ideal c/a ratio (i.e., via lattice strain) lead only to small corrections for N (< 0.1) in the thin-film limit. Similarly the epitaxial strain would not noticeably alter the demagnetization factor. Instead, it is suggested that a new strain-dependent energy term in the Hamiltonian of the epitaxial systems gives rise to a modified demagnetizing field. For example, Chappert and Bruno[38] propose that surface roughness leads to "dipolar surface anisotropy" which reduces the demagnetizing energy. Though this energy term is too small to account for the observed reduction of N in the epitaxial Er systems, a similar strain-dependent anisotropy contribution might be responsible.

VI. CONCLUSION

From the data presented here it is evident that the temperature and field dependence of the magnetic phases in the erbium films and Er/Y superlattices differ significantly from bulk Er. For example, the zero-field transition to the conical ferromagnetic state is suppressed in Er films up to 14 500 Å thick. In addition, the critical fields for all of the epitaxial samples are significantly larger than the bulk values.

Because the magnetic properties of both the superlattices and thin films are modified in a consistent fashion, it appears that the coherent growth of the Er on the mismatched Y layers is primarily responsible. Diffraction measurements indicate that the Er lattice is stretched in the basal plane and compressed along the c axis in even the thickest Er films. Only a 3950-Å film, grown on a miscut substrate, has a- and c-axis parameters that virtually match bulk Er. Thus the degree of lattice strain in the epitaxial systems is sensitive to both the relative amount of Er as well as the growth conditions. It appears that the Y/Er layers are elastically coupled during growth. On subsequent cooling, the films become locked to the substrate and do not undergo the usual magnetoelastic distortions.

We have demonstrated that the suppression of the ferromagnetic transition and the enhancement of the critical fields follow from the strain dependence of the magnetostriction. The driving energy for the transition, calculated by including the effects of the elastic coupling of the Er lattice to the Y, varies linearly with strain and is indeed consistent with the experimental critical fields.

Thus the rich magnetic behavior of bulk erbium can be tailored merely by the introduction of uniform lattice strain. The strain effects are far more significant than even the artificial modulation. The companion paper[4] details other magnetic properties of these systems, such as the modification of the nature and stability of the commensurate Er spin states, that are a direct result of the strain-induced changes of the exchange interaction.

ACKNOWLEDGMENTS

The work at the University of Illinois was supported through the National Science Foundation under National Science Foundation Grant Nos. DMR-85-21616 and DMR-88-20888. We are indebted to Jens Jensen and Alan Mackintosh for discussions of the peculiar nature of the exchange interaction in erbium.

APPENDIX: Er ELASTIC AND MAGNETOELASTIC COEFFICIENTS

The following table lists the elastic coefficients for bulk Er extrapolated from measurements by Rosen.[35] The units for these coefficients are 10^4 J/cm^3:

c_{11}	8.75
c_{12}	2.65
c_{33}	8.35
c_{13}	2.05

The temperature dependence of the lattice strains for bulk Er was measured by Rhyne and Legvold.[18] The strains above and below T_C are listed in the following table in units of 10^{-3} cm/cm:

	$T < 20$ K	$T > 20$ K
ϵ_{xx}	−1.74	−0.593
ϵ_{yy}	−1.81	−0.774
ϵ_{zz}	5.94	3.03

K_j can then be calculated from Eq. (9), which follows from the minimization of the magnetoelastic energy. The resulting coupling constants are listed in the following table in units of J/cm^3:

	$T < 20$ K	$T > 20$ K
$K_x + K_y$	−161	−31.6
K_z	423	225

*Present address: National Institute of Standards and Technology, Gaithersburg, MD 20899.

[1] J. Kwo, E.M. Gyorgy, D.B. McWhan, M. Hong, F.J. DiSalvo, C. Vettier, and J.E. Bower, Phys. Rev. Lett. **55**, 1402 (1985).

[2] R.W. Erwin, J.J. Rhyne, M.B. Salamon, J. Borchers, Shantanu Sinha, R. Du, J.E. Cunningham, and C.P. Flynn, Phys. Rev. B **35**, 6808 (1987); M.B. Salamon, Shantanu Sinha, J.J. Rhyne, J.E. Cunningham, R.W. Erwin, J. Borchers, and C.P. Flynn, Phys. Rev. Lett. **56**, 259 (1986).

[3] A. Barthelemy, A. Fert, M.N. Baibich, S. Hadjoudj, F. Petroff, P. Etienne, R. Cabanel, S. Lequien, F. Nguyen Van Dau, and G. Creuzet, J. Appl. Phys. **67**, 5908 (1990).

[4] J.A. Borchers, M.B. Salamon, R.W. Erwin, J.J. Rhyne, G.J. Nieuwenhuys, R.R. Du, C.P. Flynn, and R.A. Beach (unpublished).

[5] J.W. DuMond and J.P. Youtz, Phys. Rev. **48**, 703 (1935).

[6] M.S. Blois, J. Appl. Phys. **26**, 975 (1955).

[7] E.M. Gyorgy, D.B. McWhan, J.F. Dillon, Jr., L.R. Walker, and J.V. Waszczak, Phys. Rev. B **25**, 6739 (1982).

[8] Ivan K. Schuller, Phys. Rev. Lett. **44**, 1597 (1980).

[9] S.M. Durbin, J.E. Cunningham, M.E. Mochel, and C.P. Flynn, J. Phys. F **11**, L223 (1981).

[10] J. Kwo, D.B. McWhan, M. Hong, E.M. Gyorgy, L.C. Feldman, and J.E. Cunningham, in *Layered Structures, Epitaxy and Interfaces*, edited by J.H. Gibson and L.R. Dawson, MRS Symposia Proceedings No. 37 (Materials Research Society, Pittsburgh, 1985), p. 509.

[11] C.F. Majkrzak, J.W. Cable, J. Kwo, M. Hong, D.B. McWhan, Y. Yafet, J.V. Waszczak, and C. Vettier, Phys. Rev. Lett. **56**, 2700 (1986).

[12] J. Borchers, Shantanu Sinha, M.B. Salamon, R. Du, C.P. Flynn, J.J. Rhyne, and R.W. Erwin, J. Appl. Phys. **61**, 4049 (1987).

[13] F.H. Spedding and J.J. Croat, J. Chem. Phys. **59**, 2451 (1973).

[14] S.H. Liu, R.P. Gupta, and S.K. Sinha, Phys. Rev. B **4**, 1100 (1971).

[15] H.R. Child, W.C. Koehler, E.O. Wollan, and J.W. Cable, Phys. Rev. **138**, A1655 (1965).

[16] W.C. Koehler, J. Appl. Phys. **36**, 1078 (1965).

[17] M. Habenschuss, C. Stassis, S.K. Sinha, H.W. Deckman and F.H. Spedding, Phys. Rev. B **10**, 1020 (1974).

[18] J.J. Rhyne and S. Legvold, Phys. Rev. **140**, A2143 (1965).

[19] J.L. Feron, Ph.D. thesis, Grenoble, 1969, as referenced in B. Coqblin, *The Electronic Structure of Rare-Earth Metals and Alloys: the Magnetic Heavy Rare Earths* (Academic, New York, 1977), p. 451-457.

[20] C.P. Flynn, J.A. Borchers, R.T. Demers, R-R Du, J.A. Dura, M.V. Klein, S.H. Kong, M.B. Salamon, T-F Tsui, S. Yadavalli, X. Zhu, H. Zabel, J.E. Cunningham, R.W. Erwin, and J.J. Rhyne, in Proceedings of the MRS Conference on Advanced Materials, Tokyo, 1988, edited by Yamamoto Ryoichi [J. Phys. (Paris) Colloq. (to be published)].

[21] *International Tables for X-ray Crystallography, Volume III*, edited by James A. Ibers and Walter C. Hamilton (Kynoch, Birmingham, 1974), p. 157-163.

[22] U.W. Arndt and B.T.M. Willis, *Single Crystal Diffractometry* (Cambridge University Press, Cambridge, 1966), p. 278-279.

[23] J.D. Axe and J.B. Hastings, Acta Crystallogr. A **39**, 593 (1983).

[24] G.E. Bacon, *Neutron Diffraction* (Clarendon, Oxford, 1975), p. 38.

[25] *International Tables for X-ray Crystallography, Volume IV*, edited by James A. Iber and Walter C.Hamilton (Kynoch, Birmingham, 1979), p. 81.

[26] M. Blume, A.J. Freeman, and R.E. Watson, J. Chem. Phys. **37**, 1245 (1962).

[27] R.W. Erwin, J.J. Rhyne, J. Borchers, M.B. Salamon, R. Du, and C.P. Flynn, J. Appl. Phys. **63**, 3461 (1988); R.W. Erwin, J.J. Rhyne, J. Borchers, M.B. Salamon, R. Du, and C.P. Flynn, J. Phys. C **8**, 1631 (1988).

[28] J.A. Borchers, Ph.D. thesis, University of Illinois, 1990 (unpublished).

[29] J.A. Borchers, G. Nieuwenhuys, M.B. Salamon, C.P. Flynn, R. Du, R.W. Erwin, and J.J. Rhyne, J. Phys. C **8**, 1685 (1988).

[30] F.J. Darnell, Phys. Rev. **132**, 1098 (1963).

[31] V.A. Finkel and V.V. Vorobev, Kristallografiya **13**, 550 (1968) [Sov. Phys. Crystallog. **13**, 457 (1968)].

[32] In the sample designation $[\mathrm{Er}_n\,|\mathrm{Y}_m]_l$, n refers to the number of Er layers per bilayer, m is the number of Y layers per bilayer, and l is the total number of bilayers in the sample.

[33] J.A. Borchers, M.B. Salamon, R. Du, C.P. Flynn, J.J. Rhyne, and R.W. Erwin, J. Appl. Phys. **63**, 3458 (1988).

[34] Earl Callen and Herbert B. Callen, Phys. Rev. **139**, A455 (1965).

[35] M. Rosen, D. Kalir, and H. Klimker, Phys. Rev. B **8**, 4399 (1973).

[36] Jens Jensen (private communication).

[37] R.W. Erwin, J.J. Rhyne, J. Borchers, M.B. Salamon, R. Du, and C.P. Flynn, in *Neutron Scattering for Materials Science*, edited by S. M. Shapiro, S. L. Moss, and J. D. Jorgensen, MRS Symposia Proceedings No. 166 (Materials Research Society, Boston, 1989), p. 133.

[38] C. Chappert and P. Bruno, J. Appl. Phys. **64**, 5736 (1988).